



# Brief communication : Delayed Ice Avalanches Triggered by Earthquakes: A Strain-rate Dependent Strengthening Mechanism

Xuanmei Fan<sup>1</sup>, Shaochi Peng<sup>1</sup>, Wensong Wang<sup>1</sup>, Qing Pan<sup>1</sup>

<sup>1</sup>State Key Laboratory of Geohazard Prevention and Geoenvironment Protection, Chengdu University of Technology, Chengdu, 610059, China

Correspondence to: Xuanmei Fan (fxm\_cdut@qq.com)

**Abstract.** Earthquakes have long been regarded as one of the major triggers of ice avalanches (IAs). However, their role in IA initiation remains controversial. Here, we compiled 169 IA events that occurred between 1941 and 2022 together with their associated earthquake records, and found that only 9 IAs occurred on the same day as the earthquake. This indicates a pronounced delayed response of IAs to seismic forcing. Taking the Hailuoguo, Yanzigou, and Dagongba glaciers on Mt Gongga as examples, and using the 5 September 2022 Luding earthquake as the dividing point, we analysed glacier surface velocities during September-December 2021 and September-December 2022. The results show that glacier motion reached its maximum 1 month after the earthquake. By comparing meteorological data from the pre- and post-earthquake periods, we excluded climate variability as the primary cause of the observed glacier acceleration, thereby confirming the statistical pattern of delayed earthquake-induced IAs. We further propose a new contact model showing that seismic loading can transiently enhance the strength of ice. This strengthening effect is interpreted as the fundamental reason for the delayed occurrence of IAs after earthquakes. This study provides a new theoretical framework and fresh insights into the failure mechanism and hazard mitigation of earthquake-induced IAs.

## 1 Introduction

An ice avalanche (IA) is a glacier collapse phenomenon. Among cryospheric geohazards, IAs are an important source of material for secondary hazards such as debris flows (Kääb et al., 2018), glacial lake outburst floods (Zhang et al., 2018), and river blockages (Shugar et al., 2021). With the rapid expansion of railways, highways, hydropower stations, and other engineering projects in high mountain regions, IAs and their cascading hazards have posed increasing threats to the safe operation of such infrastructure (Kääb et al., 2018; Shugar et al., 2021; Zhang et al., 2018). In current IA hazard assessments, earthquakes are widely regarded as a key controlling factor (Zhang et al., 2023). This is especially true in the seismically active southeastern Tibetan Plateau, where seismic activity plays an important role in IA risk management and decision-making (Wood et al., 2024). However, because IAs are short-lived events that often occur in remote areas, they have received far less attention than many other natural hazards (Kääb et al., 2018; Lei et al., 2021; Zhao et al., 2021). As a result,



our understanding of the relationship between earthquakes and IAs remains limited. Clarifying this relationship is therefore  
30 of considerable scientific and practical importance.

At present, the role of earthquakes in triggering IAs remains highly debated. Some studies suggest that earthquakes can  
directly trigger IAs by damaging glacier termini or inducing basal slip. A representative example is the **Huascarán IA**  
**triggered by the 31 May 1970 Ms 7.9 earthquake** (Plafker and Ericksen, 1978). In contrast, other studies have argued that  
most IAs are not directly linked to earthquakes and may instead reflect only indirect or secondary effects (Shugar et al.,  
35 2021). For example, the 2017 Sedongpu IA occurred 41 d after a Ms 6.9 earthquake (Tong et al., 2018). These case studies  
indicate that earthquakes may both trigger IAs directly and exert longer-term influences that lead to delayed failure.  
Nevertheless, two fundamental questions remain unresolved: is the delayed response of IAs to earthquakes a general  
phenomenon, and what physical mechanism causes this delay?

To address these questions, we systematically compiled 169 IA events reported in the literature and in the Tibetan  
40 Plateau Data Center (TPDC; Zhang and Wang, 2022) for the period 1941-2022, together with earthquake records from the  
United States Geological Survey (USGS, 2021), in order to evaluate the generality of delayed earthquake-induced IAs. To  
complement the statistical analysis, we used the 5 September 2022 Luding earthquake as a natural dividing point and applied  
the pixel offset tracking (POT) method to analyse glacier surface velocities for three glaciers on Mt Gongga during  
**September-December 2021 (pre-earthquake) and September-December 2022 (post-earthquake)**. By comparing air  
45 temperature and precipitation during the same periods, we ruled out climate variability as the main driver of the observed  
glacier acceleration, thereby verifying the delayed influence of earthquakes on glacier instability. In addition, we developed a  
dynamic ice-strength model to analyse how earthquakes alter the mechanical behaviour of glacier ice and to reveal the  
mechanical basis of delayed IA initiation.

## 2 Relationship between Earthquakes and IAs

50 To explore the temporal relationship between earthquakes and IAs, we compiled a global dataset integrating both IA  
and seismic records. IA events were obtained from the published literature and open-access repositories, particularly the  
Tibetan Plateau Data Center (TPDC; Zhang and Wang, 2022). **To isolate glacier-only processes, rock-ice avalanche events**  
**were excluded, resulting in a total of 169 IAs.** For each IA, we identified potential triggering earthquakes that occurred  
within 300 km and within 1 year prior to the avalanche. Seismic data were obtained from the USGS earthquake catalogue.  
55 Given the high strain-rate sensitivity of ice relative to typical geotechnical materials, we adopted a lower magnitude  
threshold of  $M_s \geq 3.0$ , rather than the more conventional threshold of  $M_s \geq 4.0$  used in many earthquake-induced landslide  
studies. Using these criteria, we identified 85 earthquakes, indicating that at least 84 IAs had no immediate seismic  
association. Among the IA-earthquake pairs, only 9 events occurred on the same day as the associated earthquake, whereas  
the remaining 76 occurred weeks to months later. This pattern suggests that many earthquake-related IAs are not triggered



60 solely by coseismic ground shaking, but instead reflect delayed responses driven by time-dependent processes initiated by seismic forcing.

Some IA events in the dataset were located far from their associated earthquake epicentres, raising the possibility of weak or spurious correlations. To reduce the influence of such outliers, we adopted a fitting approach based on the empirical relationship proposed by Keefer (1984), which defines the maximum distance for earthquake-induced landslides. Because no established epicentral-distance threshold exists for IA-earthquake pairs, we considered both sample size and climatic interference. Small samples reduce statistical robustness, whereas large samples may include IAs influenced by long-term environmental forcing. To balance these effects, we selected 20 IAs that occurred within 2 months of earthquakes with magnitudes below 4.5, a subset less likely to be strongly affected by extreme climatic conditions (Fig. 1a). This subset was then used to derive a lower-bound empirical relationship between earthquake magnitude and epicentral distance (Eq. 1), which serves as a threshold for identifying plausible IA-earthquake pairs.

$$\log(R_D) = 0.60176M_s - 0.4561 \quad (1)$$

where  $M_s$  is the earthquake magnitude;  $R_D$  is the maximum distance (km) over which an IA can be triggered.

We further classified post-earthquake IAs based on  $R_D$  and conducted a 30-day interval statistical analysis of IA occurrences (Fig. 1b). The distribution of IA delay times exhibits a statistically significant normal pattern ( $p > 0.05$ ), with the highest number of events occurring within 1 to 2 months after the earthquake. This finding underscores the necessity of enhanced post- earthquake IA monitoring in the HMA, as delayed IAs may trigger cascading geohazards following seismic events.

At present, comprehensive temperature and precipitation data before and after each IA are unavailable, which limits our ability to fully distinguish whether these post-earthquake IAs were driven by delayed climatic changes or by sudden meteorological events such as intense rainfall. Nevertheless, this limitation does not undermine the statistical significance of our findings. The observed delay times display a clear concentration and approximate normality, supporting the hypothesis of a systematic delayed triggering mechanism associated with earthquakes.

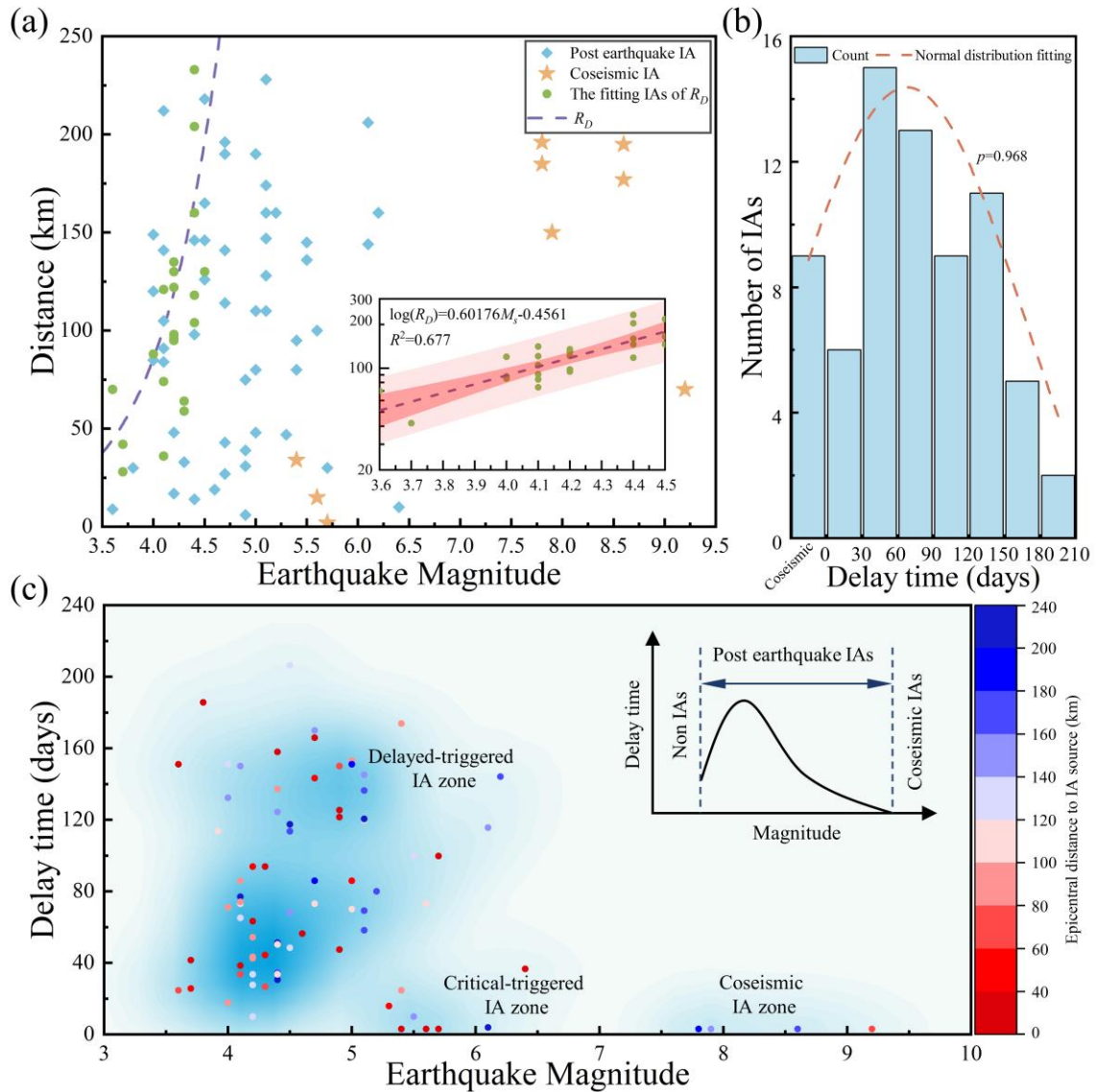


**Figure 1.** Relationship between earthquakes and IAs: (a) The distribution of epicentral distance to IA source versus the earthquake magnitude, (b) The number of IAs versus the delay time of IAs, (c) The density distribution of the delay time and IA distance versus earthquake magnitude.

85

The delay time of IAs is strongly correlated with earthquake magnitude, exhibiting distinct segmentation characteristics (Fig. 1c). No IAs were observed following earthquakes with magnitudes below 3.5. When the magnitude ranged from 4.0 to 5.0, post-earthquake IAs began to appear, and the delay time increased with earthquake magnitude. In the magnitude range of 5.3 to 6.5, both co-seismic IAs and post-earthquake IAs were recorded, with a markedly shorter delay time. When the magnitude exceeded 7.5, all observed IAs occurred co-seismically, with no delayed events.

90



95

These observations suggest a nonlinear evolution in IA delay time with increasing earthquake magnitude. Specifically, low-magnitude earthquakes ( $M_s < 3.5$ ) appear incapable of triggering IAs. As the magnitude increases, earthquakes acquire the capacity to trigger IAs, with delay time first increasing, then decreasing, and eventually approaching zero. If seismic shaking only caused structural damage to glaciers, the delay time would be expected to decrease monotonically with increasing magnitude.

### 3 Field evidence for the delayed seismic effect

100

Mt Gongga is located in the central Hengduan Mountains on the eastern margin of the Tibetan Plateau, with elevations ranging from 1420 to 7556 m and a total area of approximately 196.23 km<sup>2</sup>. Owing to favourable topographic and climatic conditions, glaciers are well developed in this region. In this study, we selected the Hailuogou and Yanzigou glaciers on the eastern slope and the Dagongba Glacier on the western slope of Mt Gongga as representative study sites (Fig. 2a). These are major glaciers in the massif and collectively reflect the geomorphic characteristics of both the eastern and western flanks. On 5 September 2022, an  $M_s$  6.8 earthquake struck Luding County, with an epicentre at 102.08° E, 29.59° N and a focal depth of 16 km. Because the epicentre was located within the Hailuogou scenic area, the potential impact of this earthquake on the glaciers of Mt Gongga attracted widespread attention.

105

Glacier surface velocity is an important indicator of glacier stability: the faster a glacier moves, the lower its stability is likely to be. Therefore, differences in glacier velocity before and after the earthquake can be used to assess the influence of seismic forcing on glacier stability. In this study, glacier surface velocities were derived using the POT method applied to interferometric wide swath SAR data from the C-band Sentinel-1A satellite. The single look complex product was used, with ascending orbit geometry, orbit number 26, frame number 93, VV polarisation, and a spatial resolution of 5 m × 20 m. According to the timing of the earthquake, the observation period was divided into a pre-earthquake interval (September-December 2021) and a post-earthquake interval (September-December 2022).

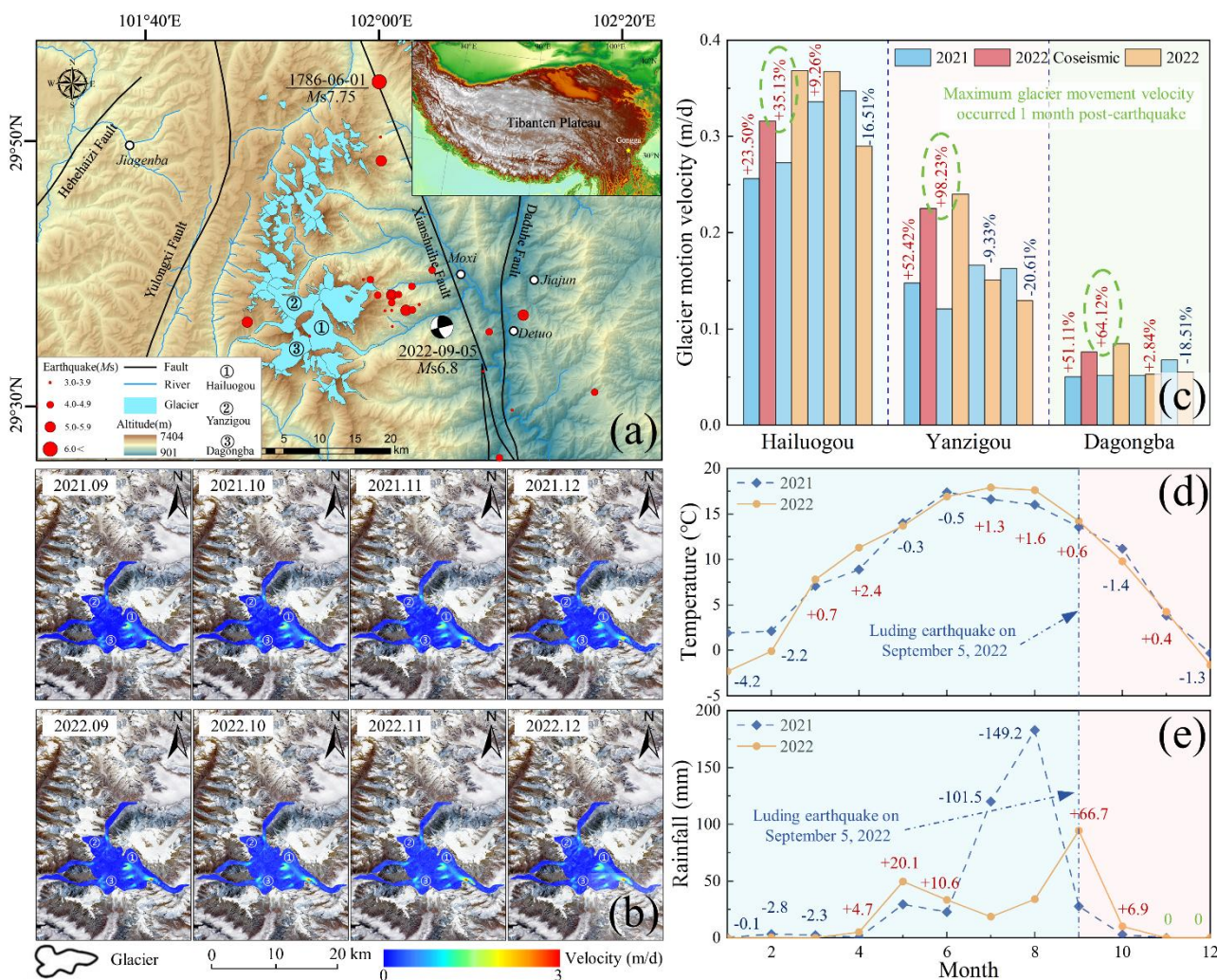
110

Figure 2b shows that during the pre-earthquake period, glacier velocity on Mt Gongga exhibited a distinct spatial pattern, with lower values in the north than in the south and in the west than in the east, and an average velocity of 0.17 m/d. Relatively strong motion signals were identified on the Hailuogou and Yanzigou glaciers. Specifically, Hailuogou Glacier reached its maximum velocity of 2.08 m/d in December, with the peak concentrated within the valley, whereas Yanzigou Glacier attained a maximum velocity of 1.45 m/d in October. In contrast, Dagongba Glacier showed only minor fluctuations in velocity, with a maximum of 0.57 m/d in December. During the post-earthquake period, Hailuogou Glacier reached a peak velocity of 2.49 m/d in November, while Yanzigou Glacier recorded a maximum of 1.74 m/d in October. Dagongba Glacier also exhibited a clear acceleration signal, with a maximum velocity of 1.40 m/d in October. Overall, glacier velocities increased markedly after the earthquake compared with the pre-earthquake period.

120

To quantify the effect of the earthquake on glacier motion, we compared the monthly mean velocities of the three glaciers during the pre- and post-earthquake periods (Fig. 2c). The results show that Hailuogou Glacier reached its maximum

velocity 1 month after the earthquake. After November, the velocities of all three glaciers declined rapidly and returned to levels comparable to those of the same months before the earthquake. **This indicates that the seismic influence on glacier motion was strongest during the first month after the earthquake and exhibited a clear delayed effect.**



**Figure 2.** Monitoring of glacier surface velocity for three representative glaciers on Mt Gongga: **(a)** Locations of the three glaciers, **(b)** Spatial distribution of glacier velocity, **(c)** Histogram of glacier velocity, **(d)** Temperature curves for the Mt Gongga region in 2021 and 2022, **(e)** Precipitation curves for the Mt Gongga region in 2021 and 2022 (Meteorological data were obtained from the National Meteorological Information Center of China. <https://data.cma.cn/>).

We further compared **temperature** (Fig. 2d) and **precipitation** (Fig. 2e) during the pre- and post-earthquake periods to assess the influence of climate variability on glacier velocity. These data were obtained from the National Meteorological Science Data Center. The temperature data show that the mean air temperature in the Mt Gongga region was 7.08 °C during the pre-earthquake period and 6.65 °C during the post-earthquake period, representing a decrease of 0.43 °C after the



135 earthquake. We can therefore exclude warming as the main cause of accelerated glacier motion. Although precipitation in  
September 2022 was significantly higher than in September 2021, this does not demonstrate that rainfall was the dominant  
cause of glacier acceleration. On the one hand, precipitation in August 2021 was much higher than in August 2022, yet no  
obvious increase in glacier velocity was observed in September 2021. On the other hand, precipitation differences between  
the pre- and post-earthquake periods were small from October to December, whereas glacier velocities differed substantially.  
140 Taken together, these observations indicate that the Luding earthquake was the main factor responsible for the  
difference in glacier motion between September-December 2021 and September-December 2022 for the three glaciers on Mt  
Gongga, whereas climatic variability had only a minor influence during this time. All three glaciers reached maximum  
velocity about 1 month after the earthquake, and these peak values were significantly higher than those recorded during the  
corresponding pre-earthquake period. This provides clear field evidence that the influence of earthquakes on glacier stability  
145 is delayed rather than purely co-seismic.

#### 4 Why do IAs exhibit a delayed response to earthquakes?

IAs involve structural failure of glacier ice, commonly leading to detachment and collapse of ice masses from bedrock.  
Under seismic loading, the mechanical behaviour of glacier ice is strongly strain-rate dependent. Laboratory experiments  
have shown that this rate dependence plays a key role in controlling the peak strength of ice. Mellor and Cole (1982)  
150 measured ice strength at low strain rates ranging from  $10^{-7}$  to  $10^{-3}$  s $^{-1}$  and found that peak strength initially increased with  
increasing strain rate up to about  $10^{-4}$  s $^{-1}$ , but then began to decrease. Subsequent studies by Schulson (1990) and Kuehn et al.  
(1993) extended this range to  $10^{-3}$  s $^{-1}$  and reported similar trends. However, this pattern does not continue indefinitely at  
higher strain rates.

Jones (1997) conducted uniaxial compression tests at strain rates between  $10^{-1}$  and  $10$  s $^{-1}$  and found that peak strength  
155 increased again with increasing strain rate, in contrast to the earlier low-rate observations. More recent low-temperature Split  
Hopkinson Pressure Bar experiments (Kim and Keune, 2007; Deng et al., 2020; Pandey et al., 2024) further confirmed that  
at high strain rates the strength of ice rises sharply and significantly exceeds values measured at low and intermediate rates.

These observations indicate that the dynamic mechanical response of ice is non-monotonic and comprises multiple  
regimes. We therefore hypothesise that this strain-rate-dependent strengthening is a key factor responsible for the delayed  
160 response of IAs to earthquakes. However, no unified mechanical framework has yet been established to describe this  
nonlinear behaviour across the full strain-rate spectrum.

##### 4.1 Strain-rate-dependent contact model

To address this gap, we propose a physically based contact model (Fig. 3a) to describe the evolution of ice strength  
under variable strain rates. The model incorporates elastic ( $k$ ), plastic ( $\sigma_f$ ), and viscous ( $\eta$ ) components arranged in a



165 series-parallel configuration to simulate inter-particle contact behaviour. As strain accumulates, the contact stress between particles can be calculated using Eq. (2), with the detailed derivation provided in Supplement S1.

$$\sigma = \frac{F}{\pi R^2} = \begin{cases} k\varepsilon^2(1 - \frac{\varepsilon}{3}) + \eta\varepsilon'\varepsilon(2 - \varepsilon), & \varepsilon \leq \frac{\sigma_f}{k} \\ \sigma_f \left[ \varepsilon(2 - \varepsilon) - \frac{\sigma_f}{k}(1 - \varepsilon) - \frac{\sigma_f^2}{3k^2} \right] + \eta\varepsilon'\varepsilon(2 - \varepsilon), & \frac{\sigma_f}{k} \leq \varepsilon \end{cases} \quad (2)$$

where  $\sigma$  is normal stress (MPa),  $F$  is contact force (N),  $R$  is ice particle radius (mm),  $\varepsilon$  is strain,  $\varepsilon'$  is strain rate ( $s^{-1}$ ),  $k$  is normal stiffness (MPa),  $\sigma_f$  is yield strength (MPa),  $\eta$  is viscosity (MPa·s).

#### 4.2 Energy partition during contact

170 Using Eq. (2), we derived the corresponding energy balance to quantify how energy evolves during deformation (Supplement S2). The total input energy is partitioned into two components: internal energy ( $U_T$ ), stored through plastic deformation, and damping energy ( $U_\eta$ ), dissipated through viscous mechanisms. In addition, the model accounts for heat exchange with the surrounding environment, described by Newton's law of cooling, in which the rate of heat transfer depends on the temperature gradient, duration, and thermal conductivity. Accordingly, the total energy during the contact  
175 process can be expressed as Eq. (3).

$$\begin{cases} U_\eta = \frac{3}{4}\eta\varepsilon'\varepsilon^2(1 - \frac{\varepsilon}{3}) \\ U_T = \frac{3}{4}e^{-\frac{\psi}{\varepsilon'}}\sigma_f \left[ \left( \varepsilon + \frac{\sigma_f}{k} \right)^2 - 4\frac{\sigma_f^2}{k^2} \right] \end{cases} \quad (3)$$

where  $U_\eta$  is damping energy density ( $J/m^3$ ),  $U_T$  is internal energy density ( $J/m^3$ ),  $\psi$  is thermal conductivity coefficient ( $K/s$ ).

#### 4.3 Strength criterion and rate dependence

180 We adopt the distortion-energy criterion (von Mises yield criterion) to relate energy accumulation to failure. Ice failure is assumed to occur when the distortion energy reaches a critical threshold. As strain rate changes, the relative contributions of damping energy and internal energy also change, thereby modifying the effective strength of the material. Using the strength at a low strain rate of  $10^{-6} s^{-1}$  as a reference, we calculated the distortion energy at different strain rates and derived a rate-dependent strength expression (Supplement S3).

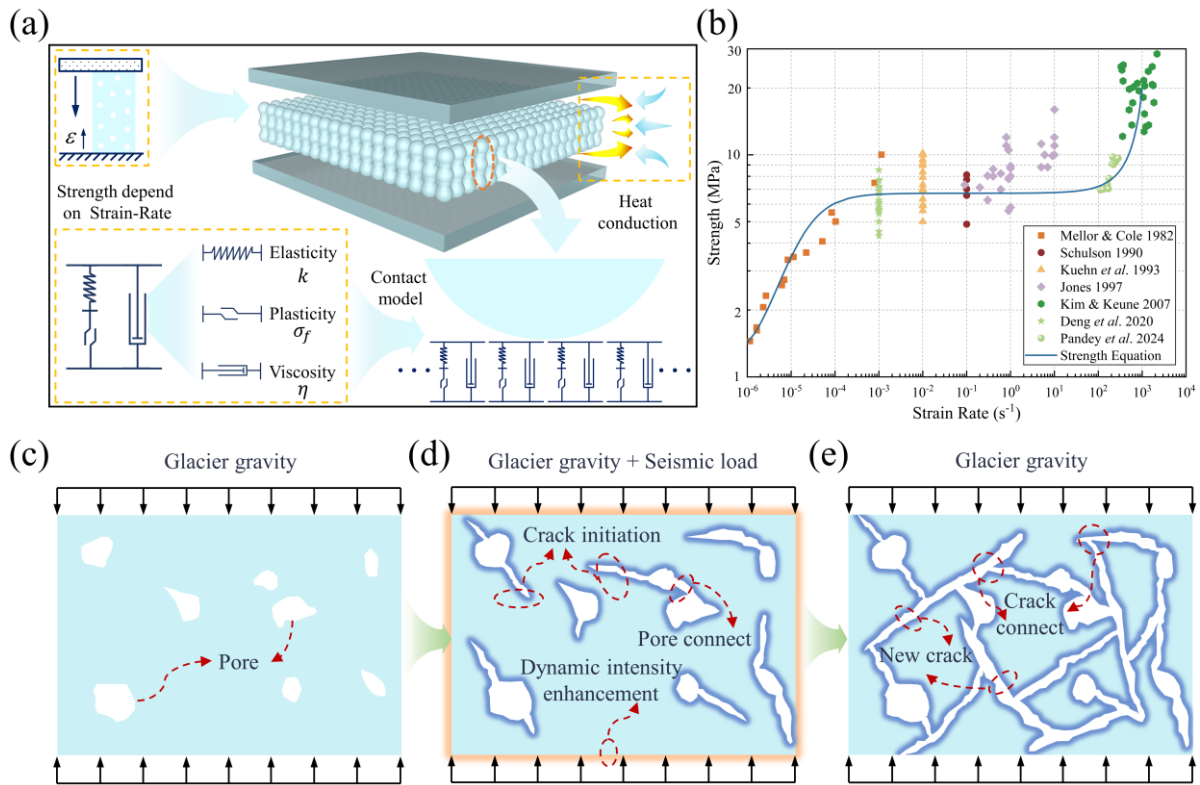


$$\frac{(1+\nu)}{3E} \sigma^2 - \frac{3}{4} e^{-\frac{\psi}{\epsilon'}} \sigma_f \left[ \left( \epsilon + \frac{\sigma_f}{k} \right)^2 - 4 \frac{\sigma_f^2}{k^2} \right] - \frac{3}{4} \eta \epsilon' \epsilon^2 \left( 1 - \frac{\epsilon}{3} \right) = \frac{(1+\nu)}{3E} \sigma_0^2 \quad (4)$$

where  $E$  is Young's modulus (MPa),  $\nu$  is Poisson's ratio,  $\sigma_0$  is reference strength (MPa).

185 To calibrate the model parameters, we compiled previously published uniaxial compressive strength data for ice over a strain-rate range of  $10^{-6}$ - $10^3$   $s^{-1}$  and temperatures between  $-15$  and  $-10$  °C (Mellor and Cole, 1982; Schulson, 1990; Kuehn et al., 1993; Jones, 1997; Kim and Keune, 2007; Deng et al., 2020; Pandey et al., 2024). Based on the mean strength values at four representative strain rates,  $10^{-6}$ ,  $10^{-3}$ , 1, and  $10^3$   $s^{-1}$ , we obtained optimal values for the normal stiffness ( $k = 28200$  MPa), yield strength ( $\sigma_f = 75.1$  MPa), viscosity ( $\eta = 7000$  Pa·s), and thermal conductivity coefficient  
190 ( $\psi = 2 \times 10^{-6}$  K/s) of the contact model.

These meso-scale parameters are substantially larger than macroscopic ice properties because they are defined at the particle scale. At the microscale, force is transmitted through discrete contact points between particles, and pores reduce the effective load-bearing area. As a result, local contact stresses are higher than bulk-averaged stresses, leading to elevated fitted parameter values. To verify their physical reasonableness, numerical upscaling was performed. Integrating the elastic  
195 stiffness over the entire domain yields a macroscopic Young's modulus of approximately 14 GPa, which is consistent with published values for glacier ice. Similarly, the contact-model yield strength estimated using a strain inflection point of 0.267 % at a strain rate of  $10^{-6}$   $s^{-1}$  is 75.1 MPa, which agrees well with experimental observations.



200 **Figure 3.** Mechanism of delayed ice-avalanche failure under seismic forcing: (a) Strain-rate-dependent contact model, (b) Agreement between model predictions and experimental data over a wide strain-rate range, (c-e) Conceptual stages showing the initial pore structure, seismic-induced dynamic strengthening, and post-seismic crack propagation leading to delayed failure.

205 **Figure 3b** compares the model predictions from Eq. (4) with the experimental data over ten orders of magnitude in strain rate. The model successfully reproduces both the strength level and the inflection point at which the rate dependence changes, demonstrating good predictive capability. More importantly, it captures the physical mechanism underlying strain-rate-dependent ice strength. At low strain rates ( $10^{-6}$ - $10^{-4}$   $s^{-1}$ ), internal energy accumulation dominates and contributes to strengthening. In the intermediate range ( $10^{-3}$ - $1$   $s^{-1}$ ), internal energy growth approaches a plateau whereas damping energy remains limited, leading to a strength plateau. At high strain rates ( $10^2$ - $10^4$   $s^{-1}$ ), damping energy accumulates rapidly, increasing energy dissipation and sustaining renewed strengthening.

210 Model results show that increasing strain rate enhances the mechanical strength of ice, implying that seismic loading can induce a transient strengthening effect. We propose that this dynamic strengthening is the key mechanism responsible for the delayed triggering of IAs following earthquakes. Based on this idea, we conceptualise a three-stage process leading to delayed failure (Fig. 3c-e).



In the initial state (Fig. 3c), glacier ice contains distributed micropores but remains stable under gravity. During seismic loading (Fig. 3d), elevated strain rates cause microcracks to initiate and propagate between pores, generating internal damage. At the same time, the increased strain rate transiently enhances the load-bearing capacity of the ice. This temporary strengthening compensates for the internal weakening, allowing the glacier to remain metastable even as microstructural damage accumulates. Once the seismic effect decays (Fig. 3e), the dynamic strengthening dissipates and the effective ice strength decreases. Under continued gravitational loading, residual cracks continue to propagate until catastrophic failure occurs and an IA is finally initiated.

## 5 Conclusions

Analysis of 169 IAs and their associated earthquakes from 1941 to 2022 shows that only nine IAs occurred on the day of the earthquake, whereas the vast majority were delayed by weeks to months. This statistically significant pattern indicates that glaciers exhibit a widespread hysteretic response to seismic forcing. In seismically active regions such as HMA, attention should therefore extend beyond co-seismic IA hazards to include delayed post-earthquake IAs, highlighting the need for prolonged post-earthquake monitoring and risk-management strategies.

For the three representative glaciers on Mt Gongga, maximum glacier velocity occurred approximately 1 month after the Luding earthquake and was significantly higher than during the corresponding pre-earthquake period. Comparison of temperature and precipitation before and after the earthquake indicates that climatic variability cannot explain the observed acceleration. These field observations provide further evidence that the destabilising effect of earthquakes on glaciers is delayed.

To explain this delay, we developed a strain-rate-dependent ice-strength model that demonstrates a transient strengthening effect during seismic shaking. Earthquakes can temporarily enhance the load-bearing capacity of ice, thereby delaying collapse despite the accumulation of internal microdamage. Once this strengthening effect dissipates, continued crack propagation under gravitational loading ultimately leads to failure. This mechanism provides a physical explanation for the temporal lag observed in many IA events.

## Data availability

The data associated with this manuscript, which were used to analyze the spatiotemporal relationship between earthquakes and ice avalanches, have been deposited in the Zenodo database and are publicly available via the following link.

Fan, X., Peng, S., Pan, Q., & Wang, W. (2026). Ice Avalanche Database from 1941 to 2022 and Seismic Records within 300 km of the Epicenter in the Preceding Year [Data set]. Zenodo. <https://doi.org/10.5281/zenodo.18856962>



### Author contributions

XF, SP QP and WW conceived and designed the research. XF processed and analyzed data. All authors participated in the writing of the manuscript.

### 245 Competing interests

The contact author has declared that none of the authors has any competing interests.

### Disclaimer

Copernicus Publications remains neutral with regard to jurisdictional claims made in the text, published maps, institutional affiliations, or any other geographical representation in this paper. While Copernicus Publications makes every effort to include appropriate place names, the final responsibility lies with the authors. Views expressed in the text are those of the authors and do not necessarily reflect the views of the publisher.

### Financial support

This research is financially supported by the Funds for National Science Fund for Distinguished Young Scholars of China (Grant No. 42125702) and National Natural Science Foundation of China (Grant No. 42572370). Sichuan Science and Technology Program (Grant No. 2026NSFSC0258; 2024ZDZX0020). Special Support Program for Cultivating Outstanding Young Scholars (Grant No. 40100-000526-01). State Key Laboratory of Geohazard Prevention and Geoenvironment Protection Independent Research Project (Grant No. SKLGP2024Z015). This work has been supported by the New Cornerstone Science Foundation through the XPLOER-2022-1012.

### References

- 260 Deng, K., Feng, X., Tan, X., and Hu, Y.: Experimental research on compressive mechanical properties of ice under low strain rates, *Materials Today Communications*, 24, 101029, <https://doi.org/10.1016/j.mtcomm.2020.101029>, 2020.
- Jones, S. J.: High strain-rate compression tests on ice, *The Journal of Physical Chemistry B*, 101(32), 6099-6101, <https://doi.org/10.1021/jp963162j>, 1997.
- 265 Kääb, A., Leinss, S., Gilbert, A., Bühler, Y., Gascoïn, S., Evans, S. G., and Yao, T.: Massive collapse of two glaciers in western Tibet in 2016 after surge-like instability, *Nature Geoscience*, 11(2), 114-120, <https://doi.org/10.1038/s41561-017-0039-7>, 2018.



- Keefer, D. K.: Landslides caused by earthquakes, *Geological Society of America Bulletin*, 95(4), 406-421, [https://doi.org/10.1130/0016-7606\(1984\)95&lt;406:LCBE&gt;2.0.CO;2](https://doi.org/10.1130/0016-7606(1984)95&amp;lt;406:LCBE&gt;2.0.CO;2), 1984.
- Kim, H., and Keune, J. N.: Compressive strength of ice at impact strain rates, *Journal of materials science*, 42(8), 2802-2806, <https://doi.org/10.1007/s10853-006-1376-x>, 2007.
- 270 Kuehn, G. A., Schulson, E. M., Jones, D. E., and Zhang, J.: The compressive strength of ice cubes of different sizes, *Journal of Offshore Mechanics and Arctic Engineering*, 115(2): 142-148, <https://doi.org/10.1115/1.2920104>, 1993.
- Lei, Y., Yao, T., Tian, L., Sheng, Y., Liao, J., Zhao, H., and Wu, G.: Response of downstream lakes to Aru glacier collapses on the western Tibetan Plateau, *The Cryosphere*, 15(1), 199-214, <https://doi.org/10.5194/tc-15-199-2021>, 2021.
- 275 Mellor, M., and Cole, D. M.: Deformation and failure of ice under constant stress or constant strain-rate, *Cold Regions Science and Technology*, 5(3), 201-219, [https://doi.org/10.1016/0165-232X\(82\)90015-5](https://doi.org/10.1016/0165-232X(82)90015-5), 1982.
- Pandey, S., Sharma, I., and Parameswaran, V.: High strain-rate behavior of polycrystalline and granular ice: An experimental and numerical study, *Cold Regions Science and Technology*, 227, 104295, <https://doi.org/10.1016/j.coldregions.2024.104295>, 2024.
- 280 Plafker G., and Ericksen G. E.: Nevados Huascarán avalanches, Peru, *Developments in Geotechnical Engineering*, Elsevier, 1978, 14: 277-314, <https://doi.org/10.1016/B978-0-444-41507-3.50016-7>, 1978
- Schulson, E. M.: The brittle compressive fracture of ice, *Acta Metallurgica et Materialia*, 38(10), 1963-1976, [https://doi.org/10.1016/0956-7151\(90\)90308-4](https://doi.org/10.1016/0956-7151(90)90308-4), 1990.
- Shugar, D. H., Jacquemart, M., Shean, D., Bhushan, S., Upadhyay, K., Sattar, A., and Westoby, M. J.: A massive rock and ice avalanche caused the 2021 disaster at Chamoli, Indian Himalaya, *Science*, 373(6552), 300-306, <https://doi.org/10.1126/science.abh4455>, 2021.
- 285 Tong, L., Tu, J., Pei, L., Guo, Z., Zheng, X., Fan, J., and Chen, H.: Preliminary discussion of the frequently debris flow events in Sedongpu Basin at Gyalaperi peak, Yarlung Zangbo River, *Journal of Engineering Geology*, 26(6), 1552-1561, <https://doi.org/10.13544/j.cnki.jeg.2018-401>, 2018.
- 290 USGS.: Earthquake catalog search. Retrieved from <https://earthquake.usgs.gov/earthquakes/search/>, 2021.
- Wood, J. L., Harrison, S., Wilson, R., Emmer, A., Kargel, J. S., Cook, S. J., and Yarleque, C.: Shaking up assumptions: earthquakes have rarely triggered Andean glacier lake outburst floods, *Geophysical Research Letters*, 51(7), e2023GL105578, <https://doi.org/10.1029/2023GL105578>, 2024.
- Zhang, T., Li, B., Gao, Y., Gao, H., and Yin, Y.: Massive glacier-related geohazard chains and dynamics analysis at the Yarlung Zangbo River downstream of southeastern Tibetan Plateau, *Bulletin of Engineering Geology and the Environment*, 82(11), 426, <https://doi.org/10.1007/s10064-023-03423-w>, 2023.
- 295 Zhang, T., and Wang, W. (2022): Global Inventory of Glacier-Related Slope Failures and Moraine Dammed Lake Outburst Floods (1901–2020), National Tibetan Plateau Data Center: Beijing, China, <https://doi.org/10.11888/Cryos.tpdc.272812>, 2022.



- 300 Zhang, Z., Liu, S., Zhang, Y., Wei, J., Jiang, Z., and Wu, K.: Glacier variations at Aru Co in western Tibet from 1971 to 2016 derived from remote-sensing data, *Journal of Glaciology*, 64(245), 397-406, <https://doi.org/10.1017/jog.2018.34>, 2018.
- Zhao C, Yang W, Westoby M, An B, Wu G, Wang W, Wang Z, Wang Y, and Dunning S.: Brief communication: A~ 50 Mm 3 ice-rock avalanche on 22 March 2021 in the Sedongpu valley, southeastern Tibetan Plateau, *The Cryosphere Discussions*, 2021: 1-1, <https://doi.org/10.5194/tc-16-1333-2022>, 2021.